Fluorescence intensity and lifetime imaging of lipofuscin-like autofluorescence for label-free predicting clinical drug response in cancer

Yinghan Yan [a,d,1], Fuqiang Xing [a,b,c,d,e,1], Jiayue Cao [a], Yiling Hu [a], Ling Li [a], Zhengyin Gao [b], Hao Jia [a,d], Kai Miao [b,c,d], Fangyuan Shao [a], Chu-Xia Deng [b,c,d,****], Kathy Qian Luo [b,d,***], Leo Tsz on Lee [b,d,**], Tzu-Ming Liu [a,d,*]

[a] Institute of Translational Medicine, Faculty of Health Sciences, University of Macau, Taipa, Macao SAR, China
[b] Cancer Centre, Faculty of Health Sciences, University of Macau, Taipa, Macau SAR, China
[c] Centre for Precision Medicine Research and Training, Faculty of Health Sciences, University of Macau, Macau SAR, China
[d] MOE Frontiers Science Center for Precision Oncology, University of Macau, Taipa, Macau SAR, China
[e] Guangdong Provincial Key Laboratory of Biomedical Imaging and Guangdong Provincial Engineering Research Center of Molecular Imaging, The Fifth Affiliated Hospital, Sun Yat-sen University, Zhuhai, China

ABSTRACT

Conventional techniques for *in vitro* cancer drug screening require labor-intensive formalin fixation, paraffin embedding, and dye staining of tumor tissues at fixed endpoints. This way of assessment discards the valuable pharmacodynamic information in live cells over time. Here, we found endogenous lipofuscin-like autofluorescence acutely accumulated in the cell death process. Its unique red autofluorescence could report the apoptosis without labeling and continuously monitor the treatment responses in 3D tumor-culture models. Lifetime imaging of lipofuscin-like red autofluorescence could further distinguish necrosis from apoptosis of cells. Moreover, this endogenous fluorescent marker could visualize the apoptosis in live zebrafish embryos during development. Overall, this study validates that lipofuscin-like autofluorophore is a generic cell death marker. Its characteristic autofluorescence could label-free predict the efficacy of anti-cancer drugs in organoids or animal models.

1. Introduction

Apoptosis is a frequently occurring and tightly regulated process for the maintenance of tissue homeostasis. Dysregulation of apoptosis may lead to uncontrolled proliferation and malignant tumors. Cancer treatment relies on therapeutic compounds or cells that trigger the apoptosis pathway [1–3]. With more understanding of cell death mechanisms, several biochemical features, such as DNA fragmentation, membrane alterations, and caspase activity, have been exploited to detect dying and dead cells. However, these approaches require fixation and staining of tissues, which limits the possibility of time-course evaluation [4]. To visualize the pharmacodynamics and the apoptosis response, scientists have designed live-cell staining probes such as peptide-tailored gold nanoclusters and recombinant substrate proteins [5,6]. All these reporter assays relied on exogenous reagents, synthetic nanoprobes, or complicated transfection protocols [7], which may alter the physiology of cells under test. Alternatively, endogenous fluorophores such as tryptophan, NADH, and flavins in cells may enable quick and label-free evaluation of cell senescence [8–10]. However, these metabolic fluorophores are nonspecific to the cell senescence process and are easily affected by other metabolic activities. Drug sensitivity tests need a background-free endogenous fluorophore that could specifically mark the cell death events. Lipofuscin is a brown-yellow, autofluorescent pigmented granules that accumulates in cells during aging [11]. In the past, lipofuscin has been widely used to report the degeneration of the retina [12], neurons [13], cardiac muscles [14], and human

mesenchymal stromal cells [15]. In 2020, Jain and Bawendi's groups found that lipofuscin's near-infrared (NIR) fluorescence could serve as a diagnostic hallmark of liver injury [16]. These previous results imply that lipofuscin fluorescence may be exploited as a label-free marker to report acute cell senescence specifically.

Cell lines are widely used *in vitro* models for drug sensitivity tests in the pharmaceutical industry. They need cumbersome fixation and staining processes to validate cell death and evaluate toxicity dosages. However, the clinical relevance of cell lines remains highly controversial [17]. Three-dimensional (3D) cell culture models, such as spheroids or organoids, could mimic the organ's microenvironment characteristics and enhance the hit rate in drug screening [18]. But organoids contain multiple cell types and scaffold structures. Especially in precision cancer medicine, these spheroids and patient-derived organoids (PDOs) are usually established from the clinical tissues of cancer patients with diverse genetic backgrounds and tissue remodeling. The temporal endpoints and effective dosages of drug screening may have large individual variations. In this situation, label-free cell death detection technique could optimize the endpoint evaluation by continuous pharmacodynamics monitoring. Recently, we further developed three-dimensional tumor slice culture (3D-TSC) model to preserve the tumor microenvironment and immune cells [19]. This model is promising for evaluating immune-checkpoint-blockade (ICB) therapy and accelerating cancer immunotherapy in personalized medicine. The label-free cell death detection technique will be even more valuable for such high-complexity drug screening models.

In the present study, we found that the cell death process induces acute red autofluorophore accumulation. Its characteristic red autofluorescence could non-invasively assess the pharmacodynamics of anticancer drugs and identify apoptosis in zebrafish's embryo development. Lifetimes of red autofluorescence could further differentiate between necrosis and apoptosis during drug treatment. These spectroscopy features of lipofuscin can potentially improve the throughput of drug screening and enable the time-course characterization of apoptosis *in vivo*.

2. Materials and methods

2.1. Cell culture

We cultured MDA-MB-231 human breast cancer cells and L929 mouse fibroblasts for cell viability and drug sensitivity experiments. The cells were maintained in a confocal dish (NEST, 801006) and incubated in a 5% CO_2 incubator at 37 °C with Dulbecco's modified Eagle's medium (DMEM) (Gibco), which contained 10% fetal bovine serum (FBS) and 1% penicillin-streptomycin (Gibco). The cells were seeded at a 5×10^5 cells/mL concentration on a glass-bottom Petri dish and cultured to 60–80% confluence for drug treatment.

2.2. Drug treatment of 2D cell cultures

To induce cell apoptosis, we treated MDA-MB-231 cells with 300 μM H_2O_2 for 6 h or 30 μM cisplatin (Sigma) for 72 h. Since L929 cells have a lower drug tolerance, they were incubated with 30 μM cisplatin for 24 h. Then, MDA-MB-231 cells were treated with different concentrations (1, 5, 10, 30, and 60 μM) of cisplatin for three batches of dose- and time-dependence experiments. To induce apoptosis related to the endoplasmic reticulum (ER) stress, we used thapsigargin (200 nM; Tocris Bioscience) to treat MDA-MB-231 cells for 48 h. To cause cell necrosis, we treated MDA-MB-231 cells with high-concentration (1 mM) H_2O_2 or 5 μg/mL shikonin (Sigma) for 6 h.

2.3. Spheroid culture

For microscopy observation, 24-well confocal plates (NEST, 801006) were coated with a 0.5% agarose scaffold to allow the formation of cancer spheroids. One hundred ovarian cancer OVCA429 cells were seeded into each pre-coated well and cultured in 500 μL of DMEM with 10% FBS and 1% penicillin-streptomycin for 3–4 days to form multicellular cancer spheroids. The spheroids were collected on Day 1, Day 2, and Day 4 after treatment with cisplatin (5 μM, 15 μM, and 30 μM) for TPF imaging and apoptosis/necrosis assays.

2.4. Three-dimensional (3D) tumor slice culture

We prepared 3D tumor slice cultures as described previously [20,21]. All animal experiments were approved by the Animal Facility of the Faculty of Health Sciences at the University of Macau (Approval number UMARE-015-2019). The tumors were harvested from genetically engineered mouse models or primary human tumors, stored in cold phosphate-buffered saline (PBS). They were cut into 200 μm thick slices with a vibratome (Leica, Biosystems Nussloch GmbH, VT1200S) within 6 h after surgery. Then, 100 μL of recombinant collagen solution was added to a Millicell insert (12 mm, Millipore, PIHP01250) and incubated at 37 °C for 20 min until solidification. Next, the slices were pre-coated with 100 μL of recombinant collagen solution and incubated at 37 °C for 20 min to solidify the top layer of tissue-containing gel. Later, a 400 μL culture medium (Ham's F12 with 20% FBS and 50 μg/ml gentamicin; Gibco) was placed into the outer inserts. Finally, the slices were incubated in a 5% CO_2 incubator at 37 °C. For the treatment groups, the cultured slices were treated with 25 μM cisplatin, anti-mouse-CD279 (αPD-1, Biolegend, 10 μg/mL) or anti-mouse-CD274 (αPD-L1, Biolegend, 10 μg/mL) for indicated days. The treated tumor slices were imaged at each time point with single-photon and multiphoton microscopy. 3-(4,5-Dimethylthiazol-2-yl)-2,5-diphenyltetrazolium bromide (MTT) was used to measure the cell viability of tumor slices. Specifically, 400 μL of 25 μg/mL MTT solution per well was used to stain the tissue slices and incubated at 37 °C for 3 h. Then, we washed away the reagent with PBS buffer and dissolved the formed formazan with 1 ml of isopropanol, followed by measurement with a plate reader (PerkinElmer Victor X3, Waltham, MA, USA) at a 570 nm wavelength. MTT images of the slices were also captured with a fluorescence stereomicroscope (Leica, M165FC, Germany).

2.5. Organoid culture

For human breast cancer organoid culture, tumor samples were obtained from Kiang Wu Hospital (approval number 20180907T), cross-cut into small pieces, and minced completely with scalpels until they were nearly liquid. For cisplatin-resistant MDA-MB-231 cell organoid culture, resistant clones were selected by gradually increasing the concentration of cisplatin. Cell lines with a high tolerance to 50 μM cisplatin were obtained [22]. RPMI medium (Gibco) with 5% FBS, collagenase I, and DNase were used for tumor digestion. After incubation at 37 °C on a shaker for 30 min to 1 h, the tumor tissue was filtered on a strainer, and the remaining suspension was centrifuged at 2000 rpm for 5 min, followed by washing with cold PBS. The cells were then mixed with Matrigel (Corning, 356234) and placed on a prewarmed 6-well cell culture plate. The prewarmed culture medium [23] was added 20 min later and changed every four days. For the confocal experiment, organoids were digested with trypsin for 10 min and pipetted gently 4–6 times every 5 min, followed by termination with serum and two washes with cold PBS. Then, the cells (6.5×10^6/mL) were mixed with cold Matrigel (10 μL) in a 24-well confocal dish at 37 °C in a 5% CO_2 incubator. The medium was added 20 min later. Normal medium or medium with different cisplatin concentrations was added on the second day for the drug sensitivity test.

2.6. Zebrafish husbandry and live imaging

The transgenic sensor zebrafishes Tg (*krt4*:sensor C3) were maintained at 28.5 °C in a ZebTEC multilinking system with a photoperiod of

14 h light to10 h dark. The zebrafish were fed with artemia twice a day. Male and female zebrafish were bred in a clean tank to get the embryos and cultured at 28.5 °C. Zebrafish larvae at 72 h post-fertilization (hpf) were used for fluorescence resonance energy transfer (FRET) imaging. The larvae were mounted with 1% low-melting agarose gel (Promega, V2111) and covered with fish water containing 0.016% MS-222 (Sigma, E10521) in an observation chamber. An 880 nm fs pulses were used to two-photon excite the apoptosis-sensing C3 proteins in the live sensor zebrafish. The CFP signals were detected at the 415–485 nm range, and the FRET YFP emissions were detected at the 506–593 nm range. The FRET images were generated by merging the corresponding CFP and YFP images. Without the caspase 3 activation, the live cells present green color in the FRET imaging. In contrast, the activated caspase 3 proteins in the apoptotic cells cleave C3 reporters and break the FRET, showing the blue color of cells in the FRET images. The TPF images of lipofuscin-like fluorescence were acquired at the same time. To avoid the co-excitation of YFP, we selectively excited the lipofuscin-like autofluorescence at 1120 nm and detected it by the PMT in a third channel (λ_{det} = 604–679 nm, red color).

2.7. Cell death analysis by flow cytometry

The apoptosis/necrosis processes of 2D cell cultures and 3D tumor models (spheroids and organoids) were characterized with an Annexin V-FITC/PI kit (Invitrogen). The harvested cells (5×10^5) were washed by PBS with gentle shaking and then resuspended in 195 μL of binding buffer. For Annexin V staining, 5 μL of Annexin V-FITC was added to the sample solution and incubated for 15 min at room temperature, protected from light. Afterward, the cells were washed with binding buffer and resuspended in 200 μL of buffer with the addition of 10 μL of propidium iodide (PI). The fluorescence signals were detected with a BD Accuri™ C6 Cytometer (BD Biosciences, USA) with standard FITC and PI channels and analyzed with FlowJo software (Tree Star). We used forward scatter (FSC), and side scatter (SSC) signals to gate and analyze at least 10000 cells in each run. Then, we obtained single-label (PI or FITC) measurements to compensate for the background signals in the FITC and PI channels. After choosing appropriate intensity thresholds, we gated the positive/negative populations for FITC and PI labeling. Healthy cells were Annexin V/PI double negative. After treatment, the apoptotic cells moved to the Annexin V-positive and PI-negative quadrant, while the necrotic (or late apoptotic) cells moved to the Annexin V/PI double-positive quadrant.

2.8. Cell death rate evaluation by the TPF of lipofuscin-like fluorescence

In each well of the same plate, we randomly selected 30 cells from bright-field images. Then, we measured the mean TPF intensity of lipofuscin-like fluorescence within cell boundaries. Since the Annexin V/PI assay reports an average 8% death rate in the control group, we set a threshold of TPF intensity at a level (2.61 counts/pixel) that could conclude a 92% survival rate in the control groups, i.e., a 92 percentile TPF level (Supplementary Fig. S6A). After treating cells with 30 μM cisplatin, we acquired 1060 nm excited TPF images at the 0, 12th, 24th, 36th, 48th, 60th, and 72nd h post-treatment. The cells with red fluorescence intensity higher than the threshold value were counted as dead, and the corresponding death rate at each timepoint was calculated (Supplementary Fig. S6B). A similar process was performed to determine the 92 percentile threshold of τ_1 fluorescence lifetime (Supplementary Fig. S6C). Estimated by a four-parameter nonlinear fitting, the threshold is 70.5 ps. The cells with a fluorescence lifetime longer than the threshold value were counted as dead and the corresponding death rate at each timepoint was calculated (Supplementary Fig. S6D).

Then, we added the photon counts of lifetime traces as another evaluation dimension. In this photon count-τ1 two-dimensional scatter plot, we performed principal component analysis to find the optimal direction, best separating live cells from apoptotic ones. For this anal-

ysis, we merged the data of the control group (30 regions) and the 48th-hour post-treatment group (20 regions). The mean photon count of the 50 regions is 1720, and the mean τ_1 is 29.4 ps. The eigenvalues λ_1 = 824537.1 and λ_2 = 485.0 of the covariance matrix give us eigenvectors $\hat{e}_1 = \begin{bmatrix} 1 \\ -0.00087 \end{bmatrix}$ and $\hat{e}_2 = \begin{bmatrix} 0.00087 \\ 1 \end{bmatrix}$, respectively. The direction of $\hat{e}_2$ could best distinguish control from the apoptosis group. So we assigned as a new index and applied it to all the measured data. For the PC2-based analysis, we concluded 21.8 as the threshold in the control group (Supplementary Fig. S6E). The cells with a PC2 index higher than the threshold value were counted as dead, and the corresponding death rate at each timepoint was calculated (Supplementary Fig. S6F).

$$PC2 = 0.00087 \times (photon\ counts) + (\tau_1\ lifetime) \tag{1}$$

Then we used a nonlinear fitting (four parameters) in Origin 2017 software to model the curve that predicts the death rate at specific observation time points (Supplementary Figs. S6B, D, F). Then we could estimate the corresponding time that could conclude 50% apoptosis rate.

2.9. In situ imaging of apoptotic cells with a caspase-3 detection kit

After imaging red autofluorescence in apoptotic cells, we used a caspase-3 detection kit (Invitrogen, Image-iT™ LIVE Green) to confirm the onset of apoptosis. The treated cells and the control cells were mixed with 30X FLICA working solution in a cell culture medium and incubated for 60 min under culture conditions. Afterward, the cells were washed twice with 1X wash buffer, and the caspase-3 distribution was imaged by confocal microscopy at an excitation wavelength of 488 nm.

2.10. Labeling of intracellular lysosomes with LysoTracker dyes

LysoTracker Green (Thermo Fisher, DND-26) was used to confirm whether stress-induced red autofluorescence accumulated in lysosomes. It was used to mark the location of lysosomes, and the relative distribution of red autofluorescence was observed simultaneously. Lyso-Tracker Green solution (75 nM) was added to the culture medium of the control and drug-treated groups. Then, the cells were incubated with the dye for 45 min at 37 °C and washed twice with PBS.

2.11. Two-photon fluorescence imaging

For TPF imaging, cells were seeded in confocal dishes and incubated in a microscope-compatible microincubator system that contained 5% CO_2 and the temperature was maintained at 37 °C (Nikon Instrument Inc., Japan). A wavelength-tunable (700–1300 nm) near-infrared femtosecond laser (InSight X3, Spectra-Physics) served as the light source for two-photon fluorescence imaging, which can extend the penetration depth and reduce photodamage to cells in 3D tumor culture. Each image was captured using a Nikon Eclipse Inverted Multiphoton Microscope (A1MP + Eclipse Ti-2E, Nikon instrument Inc., Japan) with a 40 × NA = 1.15 water-immersion objective. The excited TPF and second harmonic generation (SHG) signals were epi-collected by the same objective, reflected by a multiphoton dichroic beam splitter, and detected by four photomultiplier tubes (PMTs). Lipofuscin-like autofluorescence can be selectively excited at 1060 nm and detected by the PMT in channel 3 (λ_{det} = 604–679 nm). This excitation wavelength avoids the two-photon co-excitation of flavins or YFP. The PMT in channel 2 (λ_{det} = 506–593 nm) detected the 520 nm SHG signals of 3D tumor slices. In the wavelength-dependent excitation experiment, the laser power at different excitation wavelengths was equalized to 15 mW. For each experimental group, we captured 3 images with 317 × 317 μm fields of view, from which at least 30 cells were picked up to analyze fluorescence intensities. In addition, a CCD-cooled spectrometer (iDus 401 plus shamrock 193i, ANDOR, Oxford Instruments) was attached to

the backside port of the inverted microscope. Every time one multiphoton image was captured, we obtained the corresponding two-photon emission spectra from the integrated spectrometer.

2.12. FLIM imaging and data analysis

In the backside port of the same multiphoton microscope (Eclipse Ti-2E, Nikon), we further installed two photon-counting PMTs (PMC-150-4, Becker & Hickl) sharing the same signal light path with the fluorescence spectrometer. The fluorescence lifetime data were recorded by a time-correlated single-photon counting system (SPC-160, Becker &

Hickl) synchronized to the scanning excitation of a Nikon A1 MP + multiphoton microscope. To improve the quality of lifetime fitting, we took 120 s to acquire one FLIM image, such that the peak photon counts of lipofuscin-like fluorescence were higher than 200 for most pixels in cells. A pixel dwell time of 25.21 μs was set to obtain a 256×256 pixels image.

2.13. Statistical analysis of the intensity and lifetime of lipofuscin-like fluorescence

The mean fluorescence intensity within a cell was evaluated with Fiji
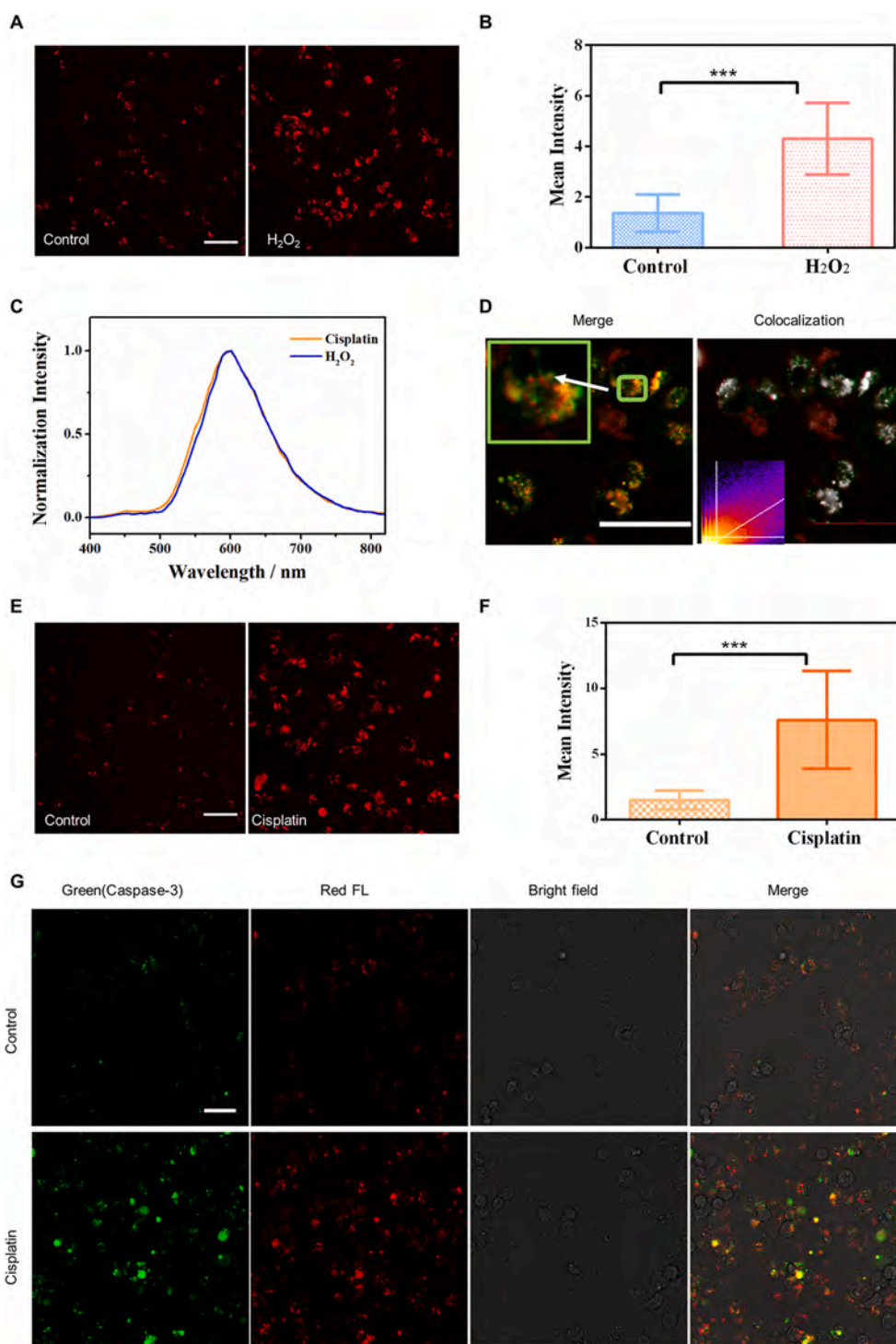

Fig. 1. Signatures of lipofuscin red fluorescence in cell apoptosis. A- B Two-photon fluorescence imaging and intracellular fluorescence intensities (n = 30) of control and H_2O_2 treated (300 μM, 24 h) MDA-MB-231 cells. $\lambda_{ex} = 1060$ nm; $\lambda_{detect} = 604$–679 nm; Scale bar: 50 μm. **C** Two-photon fluorescence spectra ($\lambda_{ex} = 1060$ nm) of red autofluorescence in cisplatin-treated (30 μM, 72 h) and H_2O_2 treated (300 μM, 24 h) MDA-MB-231 cells. **D** The colocalization of lysosomes with accumulated red autofluorophores induced by 30 μM cisplatin for 72 h. Green color: Lyso-Tracker, excited at 488 nm. Red color: lipofuscin, excited at 561 nm. White pixels represent the colocalized ones. Scale bar: 50 μm. **E-F** Two-photon fluorescence imaging and intracellular fluorescence intensities (n = 30) of control and cisplatin-treated (30 μM, 72 h) MDA-MB-231 cells. $\lambda_{ex} = 1060$ nm; $\lambda_{detect} = 604$–679 nm; Scale bar: 50 μm. The statistical mean and standard deviation (error bars) in **B** and **F** were calculated from data in three independent images acquired under the same excitation conditions. ***$p < 0.001$, student's *t*-test is used when the treated group was compared with the control group. **G** Confocal fluorescence, brightfield, and merged images of cells stained with Caspase 3-Green in the control and cisplatin-treated groups. Green represents the distribution of caspase-3, and red represents lipofuscin fluorescence. Scale bar: 50 μm.

software (ImageJ). For each group, three images were acquired, and at least 30 cells were analyzed. Lipofuscin intensity in the cell was evaluated by the mean fluorescence value within the cell cytoplasm. For the lifetime statistics, SPC Imaged software (Beker & Hickl) was used to analyze the FLIM data. The fluorescence lifetime of each pixel was fitted by a double exponential decay model $I(t) = IRF \otimes I_0(\alpha_1 e^{-t/\tau_1} + \alpha_2 e^{-t/\tau_2})$, where IRF is the instrument response function measured from the SHG of urea. α_1 and α_2 represent the amplitude percentages of the photon contributions from two-lifetime components, τ_1 and τ_2, respectively. We optimized the trace fitting to a low chi-square error, and the software generated the amplitude-weighted lifetime histogram and color-coded lifetime image. For the simplicity of comparison, sometimes we used $\tau_m = \tau_1 \times \alpha_1 + \tau_2 \times \alpha_2$ for analysis (Supplementary Fig. S18). Similar to the study of fluorescence intensity, in some FLIM images, we acquired at least three images to obtain over 30 cells (image size: 512 × 512 pixels, 0.25 μm pixel size, binning 4 × 4, amplitude with 200 photons, collection time: 120 s). We selected the boundaries of cells from the bright-field images and analyzed the corresponding lifetime properties of lipofuscin-like fluorescence. The significance of exported data was analyzed by unpaired student's *t*-test and Kruskal-Wallis test according to the sample size with GraphPad Prism software (version 6.0). Data are mean ± SD of two or three independent experiments (Supplementary Fig. S19). Two-dimensional (2D) scatter plots were obtained via Origin software (version 8.6).

3. Results

3.1. Apoptotic cells accumulate red autofluorescence derived from lysosomes

Several common drugs and cytotoxic H_2O_2 were employed to induce cell death, either apoptosis or necrosis. First, we treated MDA-MB-231 cells with H_2O_2 at an apoptotic concentration of 300 μM [24,25]. After 24 h of incubation, the Annexin-V/PI staining assay indicated cells were driven toward apoptosis (Supplementary Fig. S1A). Observed by a multiphoton microscope, these apoptotic cells exhibited a significant increase of two-photon red autofluorescence intensity excited at 1060 nm (Fig. 1A and B). The corresponding fluorescence spectrum is broad and has an emission peak at approximately 600 nm (Fig. 1C), resembling that of lipofuscin observed by the fundus camera [26]. By sweeping the two-photon excitation wavelength from 820 nm to 1240 nm at equivalent laser power, we found several effective excitation bands at 1020, 1060, and 1100 nm (Supplementary Figs. S1B–D). Confirmed by Lyso-Tracker labeling, most of these stress-induced autofluorophores accumulated in lysosomes (Fig. 1D colocalization analysis in the Supplementary Materials, Table S1, and Supplementary Fig. S2). It is well known that, in aging cells, insufficient autophagy impedes the removal of damaged mitochondria [27] and results in lipofuscin formation in the lysosome. The apoptosis-induced autofluorophores and aging-related lipofuscins [13] share the same metabolic fate. Then we applied cisplatin at an apoptotic dosage (30 μM for 72 h) to MDA-MB-231 cells (Fig. 1E and F; Supplementary Fig. S3) and L929 fibroblasts (Supplementary Fig. S4). We also observed elevated red autofluorescence with similar TPF excitation spectra and emission spectra (Fig. 1C). In addition, the caspase-3 activity detection assay kit (Caspase 3-Green) was also used to *in situ* visualize apoptotic cells. Cells stained with caspase-3 activity dye exhibited accumulated caspase-3 green fluorescence in cisplatin-treated cells while cells in control group exhibited low background green autofluorescence signal. Most of caspase-3 positive cells contain red fluorescent granules (Fig. 1G). These biochemical, spectroscopic, and microscopic evidence support the notion that stress-induced red autofluorescence is strongly correlated with the apoptosis. They might originate from the acute accumulation of lipofuscin-like fluorophore in lysosomes.

3.2. Lipofuscin-like fluorescence early reports the drug sensitivity

Based on the evidence above, we speculated that the dynamic accumulation of lipofuscin-like fluorophores might reflect the severity and heterogeneity of cell damage under drug treatment. Time-course monitoring of this hallmark autofluorescence could reveal the early pharmacodynamic signatures. To explore its potential in drug sensitivity tests, we analyzed the correlation of red autofluorescence to cell apoptosis in a time- and dose-dependent manner in cisplatin-treated MDA-MB-231 cells. With the Annexin V/PI assay (Supplementary Fig. S5A), the IC$_{50}$ dosage would be approximately 30 μM at 72 h post-treatment (Supplementary Figs. S5B–D), which indicates MDA-MB-231 cells have high tolerance to the cisplatin. Due to the overgrowth-induced cell death (Supplementary Fig. S5A), the control and sublethal groups have a constant background death rate. Examined by TPF microscopy, the control groups (0 μM, 0 h) have few red fluorescent cells in the field of view. As drug incubation time and concentration increased, the intracellular TPF intensity and density of red fluorescent cells increased (Fig. 2A and B). The increased number of red fluorescent cells at 72 h reflects the overgrowth-induced cell death.

To further test how early the apoptosis fate could be determined, we washed the drug away at the 12th and 24th h post-treatment and further cultured them in a fresh medium for 24 h. The cells still showed elevated apoptosis from 5.9% (12 h w/drug) and 12.0% (24 h w/drug) to 13.1% (12 h w/+ 24 h w/o drug) and 27.4% (24 h w/+ 24 h w/o drug), respectively (Supplementary Fig. S5E). They still followed the trend of a growing death rate after the drug withdrawal from incubation. The trend of cell apoptosis has been determined after 12 h incubation. But conventional Annexin V/PI assays need a 72 h endpoint to see the IC$_{50}$ dosage. In contrast, the lipofuscin-like autofluorescence can monitor and report the early change at the 36th hour post-treatment (Fig. 2B). To calculate the TPF-based IC$_{50}$, we set a TPF threshold of cell death based on the cell death rates of control groups in Annexin V/PI assays. Counting 30 randomly selected cells in each condition, we obtained the death rate as the function of observation time points. The fitted 50% apoptosis timepoint was 52 h, which is earlier than 72 h of Annexin V/PI assays. (Supplementary Figs. S6A–B).

Additionally, the lipofuscin-like red fluorescence lifetime could also report the state of apoptosis. The mean fluorescence lifetimes of cells increased from 171 ps before treatment to 287.7 ps at the 12 h post-treatment. They finally reached 507 ps at the 48–72 h post-treatment (Fig. 2C). Using lifetime curve fitting, we found the short component τ_1 is more sensitive to cell death (Supplementary Figs. S6C–F). For fluorescence lifetime-based IC$_{50}$, we set 42.6 ps as a threshold (Supplementary Fig. S6C) to identify the apoptotic cells with longer lifetimes. Under the τ_1 index, we could detect the 50% apoptosis rate at 52 h (Supplementary Fig. S6D).

Then we combine the photon counts of lifetime traces with τ_1, and use principal component analysis (PCA) to find an optimal index (See the Method section). In this PC2-based IC$_{50}$ analysis, we concluded 21.8 as the threshold in the control group (Supplementary Fig. S6E). The combined index concluded a 50% apoptosis rate at 55 h (Supplementary Fig. S6F).

3.3. Lifetimes of lipofuscin-like fluorescence differentiate between necrosis and apoptosis

Although the apoptosis process induces elevated lipofuscin-like fluorescence, the increased red autofluorescence does not necessarily indicate apoptosis. Other types of cell death, such as necrosis, may share the same features. Cell necrosis is uncontrolled cell death and is harmful to the surrounding cells in tissues. It was commonly observed in acutely damaged cells. Differentiating between apoptosis and necrosis is important for evaluating the therapeutic efficacy of anti-cancer drugs.

We used 1 mM H_2O_2 and 5 μg/mL shikonin [28] to induce the necrosis process in MDA-MB-21 cells. After 6 h of incubation, necrotic
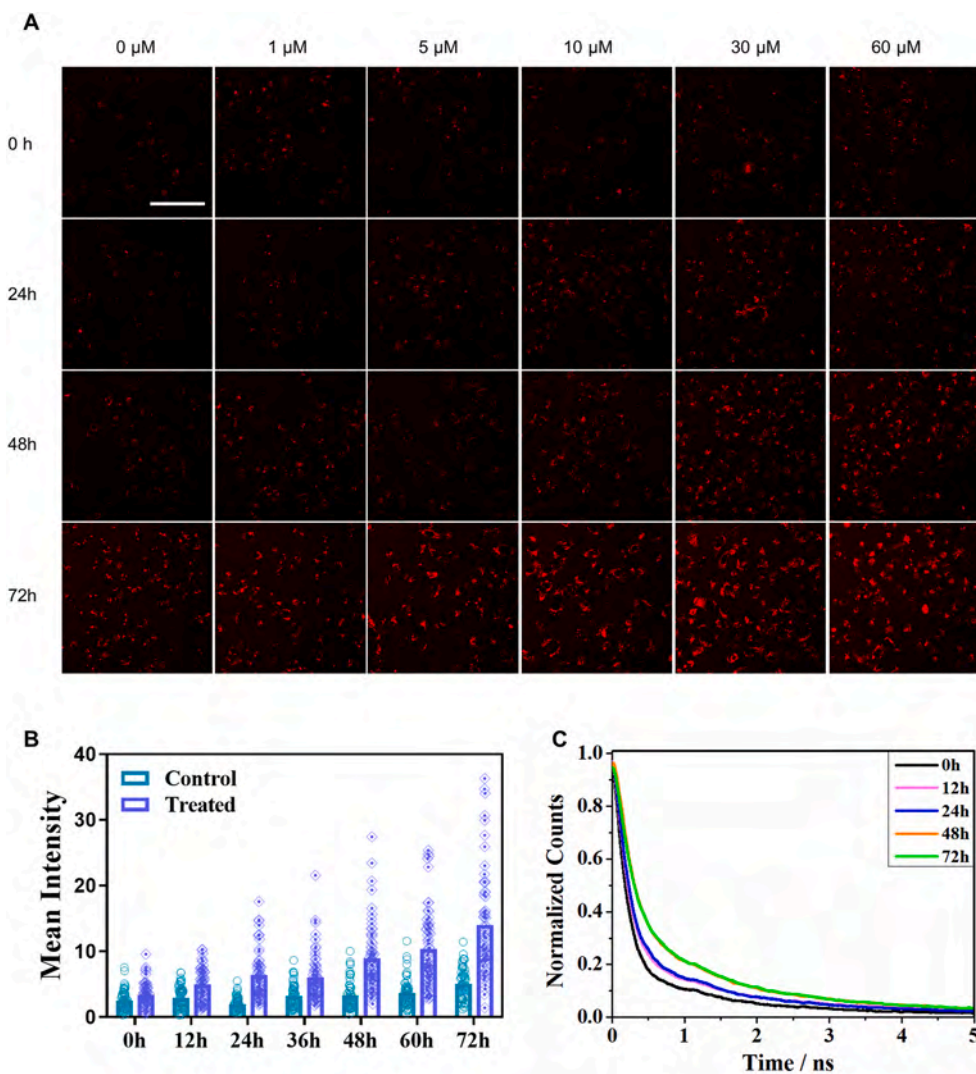
Fig. 2. Dynamic features of lipofuscin red fluorescence in apoptotic cells. A Time- and dose-dependent red autofluorescence images of 30 μM cisplatin-treated MDA-MB-231 cells. Scale bar: 100 μm. **B** Mean intensities of red autofluorescence in cells after different incubation times (n = 30). **C** Lifetime traces of cellular red autofluorescence before treatment (0 h) and at the 24th, 48th, and 72 nd h post-treatment. Data are representative of three independent experiments.

cells, on average, accounted for 46.9% and 59.5% of the population, respectively. Under these conditions, we also found significantly increased red TPF in necrotic cells (Supplementary Figs. S8 and 9). The average fluorescence intensity in shikonin-treated cells showed a significant increase at 5 μg/mL (Supplementary Fig. S9B). Their spectral shapes are similar to those of apoptotic cells. This result means that the intensity of lipofuscin-like red autofluorescence can indicate cell senescence but not the type of cell death.

To differentiate between necrosis and apoptosis, we introduce an additional parameter, the TPF lifetime of lipofuscin-like fluorescence. In contrast to intensity measurement, fluorescence lifetime measurement can avoid artifacts caused by photobleaching and requires less calibration under excitation conditions. In addition, the fluorescence lifetime can reflect the effects of environmental factors, including solution pH values, the presence of quenchers, self-aggregation, and the association with macromolecules. Suppose the increased fluorescence lifetime we observed in apoptosis results from the lysosomal environment. Then, it is reasonable to infer that the rupture of lysosomes in necrosis [29] may significantly alter the fluorescence lifetime of lipofuscin-like fluorophores.

After analyzing the fluorescence lifetime imaging microscopy (FLIM) of lipofuscin-like fluorescence in apoptotic MDA-MB-231 cells

(Supplementary Figs. S10A–D), there were two major lifetime components, $\tau_1 = 400–700$ ps and $\tau_2 = 2200$ ps, with amplitude proportions of 72% (α_1) and 28% (α_2), respectively (Supplementary Figs. S10C and D). In contrast, the fluorescence lifetime in the control group was dominated ($\alpha_1 = 88\%$) by a significantly shorter $\tau_1 = 100–300$ ps and $\tau_2 = 1500$ ps than observed under apoptosis conditions. From the α_2-τ_1 two-dimensional scatter plot, we could see that the apoptotic cells' data points separated well from those of live cells (Supplementary Fig. S10B). Then, we performed a similar measurement on L929 fibroblasts. The lifetimes of red autofluorescence in apoptotic L929 cells ($\tau_1 = 200–400$ ps; $\tau_2 = 2000$ ps) were also longer than those in control ones ($\tau_1 = 150$ ps; $\tau_2 = 1750$ ps). The α_2-τ_1 scatter plots could also separate apoptotic cells from control ones (Supplementary Figs. S10E–I).

Knowing that FLIM can distinguish apoptotic cells from normal ones, we further validated its use in differentiating between necrosis and apoptosis. Although both 1 mM H_2O_2 and shikonin induced an increase in red TPF in necrotic cells, they shortened the fluorescence decay time compared to that observed during cell apoptosis (Supplementary Figs. S11A and B). As we expected, after LysoTracker labeling, we could not find any lysosomes in necrotic cells (Supplementary Fig. S11C). We speculated that the lysosomes were severely damaged during necrosis, thus releasing the lipofuscin-likefluorophores to the cytosol

(Supplementary Fig. S11D) and altering their fluorescence lifetime.

For more solid validation, we used the ER stressors thapsigargin (TG) and cisplatin to initiate cell apoptosis and the 1 mM H_2O_2 and 5 μg/mL shikonin to induce cell necrosis. Flow cytometry confirmed the cell status with Annexin V/PI staining (Supplementary Figs. S11A and B). All treated cells showed strong red lipofuscin-like TPF at the experimental endpoints, and the color-coded FLIM of the mean lifetime τ_m (Fig. 3A) revealed the type of death. There was some necrosis (uniform yellow color) in TG-treated cells and some apoptosis (granules with cyan color) in H_2O_2-treated cells. Compared with apoptotic cells, necrotic ones showed a much shorter $\tau_1 = 200$ ps and $\tau_2 = 1300$ ps (Fig. 3B). The short-lifetime component contributed more ($\alpha_1 = 80\%$) than those of apoptotic cells (Fig. 3C). These results validate that FLIM and sub-cellular structures of lipofuscin-like TPF could label-free differentiate between necrotic cells and apoptotic ones.

To further elucidate the advantage of the fluorescence lifetime in determining the type of cell death, we treated the ovarian cancer cell line OVCA429 with 5 μM, 15 μM, and 30 μM cisplatin. As shown in Fig. 3D, a time- and dose-dependence study revealed that the red autofluorescence in OVCA429 cells increased with the cisplatin dosage and the incubation time. Interestingly, the FLIM data showed that the type of cell death is dosage-dependent (Fig. 3E and Figure S12A, B). Cells underwent apoptosis at a low dose of cisplatin (5 μM) but became necrotic at concentrations of 15 μM and 30 μM. The separation of cells of different statuses could be easily observed in the α_2-τ_1 2D scatter plots (Fig. 3F). We double-confirmed this phenomenon with specific Annexin V/PI assays (Supplementary Fig. S12C). This example demonstrates that lipofuscin-like fluorophores can reveal drug sensitivity and determine the effects of dosage on the type of cell death.

3.4. Lipofuscin-like autofluorescence reports drug responses in spheroid and organoids models

Compared to 2D cell cultures, 3D tumor models better mimic the tumor microenvironment. They express more physiologically relevant targets for reliable drug screening. However, the techniques for analyzing samples from patient-derived 3D tumor models are limited. Conventional assays require dissociation of the tissues or spheroids, which may affect the evaluation of treatment responses [30]. Various organoids may need tailored protocols of fixation and staining. For rapid and *in situ* monitoring of the treatment responses in patient-derived samples, we need label-free and non-invasive ways of cell death evaluation. Our lipofuscin-like fluorescence could provide an imaging cytometry solution to visualize the spatial distribution of treatment responses, either apoptosis or necrosis, in the cells' original living environments and niches.

As validated in Fig. 3, necrotic cells have a shorter decay time of lipofuscin-like fluorescence compared to apoptotic ones. Based on the imaging of stress-induced lipofuscin-like autofluorescence (red color in Fig. 4A) in 3D spheroid derived from OVCA429 cells, we observed the dynamics of spheroid treatment. After treatment with 5, 15, and 30 μM cisplatin, lipofuscin-like fluorescence intensity significantly increased in OVCA429 spheroid models within 2 days (Fig. 4B and Supplementary Figs. S13A and B). The lifetimes of red fluorescence in 15 and 30 μM cisplatin-treated cells were longer than those in the control groups (Fig. 4C). The imaging area of 30 μM cisplatin-treated group may contain more proportion of necrotic cells, leading to a shorter overall lifetime than 15 μM group did. It was confirmed by Annexin-V/PI staining (Supplementary Fig. S13C). Therefore, the stress-induced increase of red fluorescence and lifetimes is strongly correlated with the degree of cell senescence.

Unlike spheroids, organoids are identified as 3D cell aggregates derived from primary tissues or stem cells. They can self-renew and display organ functions [31,32]. Tumor organoids recapitulate the tumor microenvironment by maintaining the organ cell types and genetic features of the original tumors [33,34]. To identify the early

hallmarks that could determine apoptosis fate, we used our label-free optical method to achieve rapid, and time-course monitoring of an organoid model derived from a human breast tumor. Based on the imaging of lipofuscin-like fluorescence in 3D tumor organoids, we observed pharmacodynamics dependent on the cisplatin dosage (1, 5, and 30 μM) and incubation time (Supplementary Fig. S14). After treatment, we observed the increasing lipofuscin-like fluorescence intensity and lifetimes in organoids within four days (Fig. 4D–F). This cisplatin-induced red fluorescence in human tumor organoids strongly correlated with the degree of cell senescence, as confirmed by Annexin-V/PI staining. (Supplementary Fig. S14). In contrast, the organoids composed of cisplatin-resistant MDA-MB-231 cells showed no obvious intensity increase (Supplementary Figs. S15A and B). This result demonstrates that if the tumor is resistant to the treatment, the cells can handle the drug-induced stress and accumulate no lipofuscin-like red fluorescence.

3.5. Lipofuscin-like imaging quantitatively evaluates the apoptosis in 3D-tumor slice culture in situ and zebrafish's embryo development in vivo

Furthermore, we applied our lipofuscin-like reporting approach to evaluate anti-cancer drug efficacy in a three-dimensional tumor slice culture (3D-TSC) model. 3D-TSC could even preserve the tumor microenvironment and immune cells, which is critical for evaluating immune-checkpoint-blockade (ICB) therapy. By imaging drug-induced lipofuscin-like fluorophore (red channel in Fig. 5A) and collagen (green color in Fig. 5A) in cells, we investigated the 3D-TSC treatment dynamics over 4 days. After treatment with 25 μM cisplatin, 2.5 μg/mL αPD-1 (anti-PD1), and 2.5 μg/mL αPD-L1 (anti-PD-L1), we also observed enhanced lipofuscin-like fluorescence intensity in the tumor slices, and the lifetime increased to a much longer 950 ps under αPD-1 and αPD-1 treatment compared with that of the control group (573.4 ps) (Fig. 5B). However, for cisplatin treatment, the intensity and lifetime of lipofuscin-like fluorescence were slightly lower than those of the ICB therapy groups (Fig. 5B and C). This phenomenon implies that more tumor cells were eradicated by ICB therapy than by cisplatin treatment. The stress-induced red fluorescence intensity and lifetime change are well-correlated with conventional cell viability assay (Supplementary Figs. S16A and B). As a double-check, we also employed green fluorescence protein (GFP) labeled breast tumor cells to build the animal model. Over a treatment time course in 3D-TSCs, we verified that the enhancement of lipofuscin-like fluorescence intensity was accompanied by the disappearance of GFP$^+$ cells (green color in Fig. S17A). Our results validate that lipofuscin-like fluorescence could serve as a valuable optical reporter for label-free and time-course monitoring of pharmacodynamics in 3D-TSCs.

We also applied this technique to patient-derived tumor slices of colon cancer and nasopharyngeal cancer samples. There was a significant increase in lipofuscin-like fluorescence intensity in colon cancer after treatment with αPD-L1 for 7 days (Fig. 5D and E). But nasopharyngeal cancer tumor slice (NPC) showed different therapy responses between the two patients. For patient NPC-1, the lipofuscin-like fluorescence only slightly increased while αPD-L1 treated NPC-2 exhibited a significant increase (Fig. 5D–F). This practical method is translatable to clinical practice.

Finally, we further investigated the developmental apoptosis in live zebrafish to confirm that lipofuscin-like fluorescence comes from endogenous molecules, not exogenous drugs. The transgenic sensor C3 zebrafishes were established to report the cell apoptosis based on fluorescence resonance energy transfer (FRET) imaging [6,35]. When the sensor C3 was excited by 880 nm fs laser pulses, the excited charges of cyan fluorescence proteins (CFP) could transfer to the excited states of yellow fluorescence proteins (YFP) due to the FRET effect. Under this condition, most of the C3 sensors emit YFP fluorescence. During the cell apoptosis, the activated caspase-3/7 cleaved the DEVD site to disconnect the FRET-pair and recover the CFP emission (Fig. 6A). During embryonic
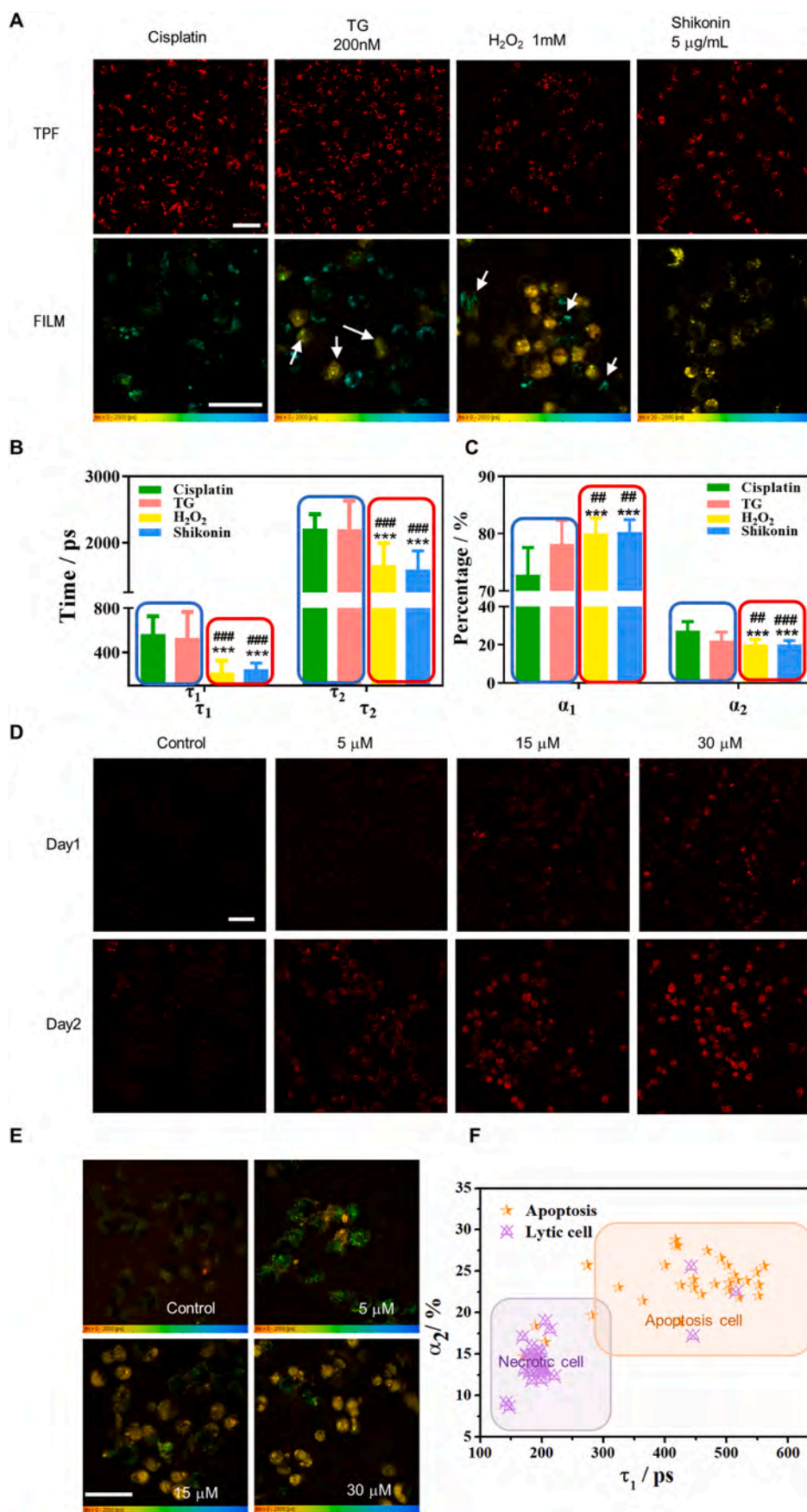
Fig. 3. Lifetime parameters of stress-induced lipofuscin autofluorescence differentiate between necrosis and apoptosis in individual cells. A Intensity (TPF) and lifetime imaging (FILM) of two-photon red autofluorescence after treatment with 30 μM cisplatin for 72 h, 200 nM TG for 48 h, and 1 mM H_2O_2 and 5 μg/mL shikonin for 6 h. The TPF and FILM images were acquired from the same samples in each group. White arrows indicate necrotic cells (uniform yellow color) in TG-treated group and apoptosis cells (granules with cyan color) in H_2O_2-treated group. Scale bars: 50 μm. B, C Comparing the lifetime parameters τ_1, τ_2, α_1, and α_2 of individual cells (n ≥ 30) treated with different inducers. ***$p < 0.001$, student's t-test when H_2O_2 and shikonin were compared with cisplatin, ###$p < 0.001$, student's t-test when H_2O_2 and shikonin were compared with TG. The blue and red frames in (B) and (C) classified the apoptosis inducers and necrosis inducers, respectively. D OVCA429 cells were treated with 5 μM, 15 μM, and 30 μM cisplatin for one and two days. E FLIM of OVCA429 cells at each dosage. Color legend: 0–2000 ps. F The τ_1-α_2 scatter plot of OVCA429 cells shows that the data points for the 5 μM dosage (orange star) largely fall within the apoptosis zone, while those for the 30 μM dosage (purple triangle with a cross) largely fall within the necrosis zone. The coordinates of each dot represent the (τ_1, α_2) values of the individual cell (n ≥ 30). Scale bar: 50 μm.
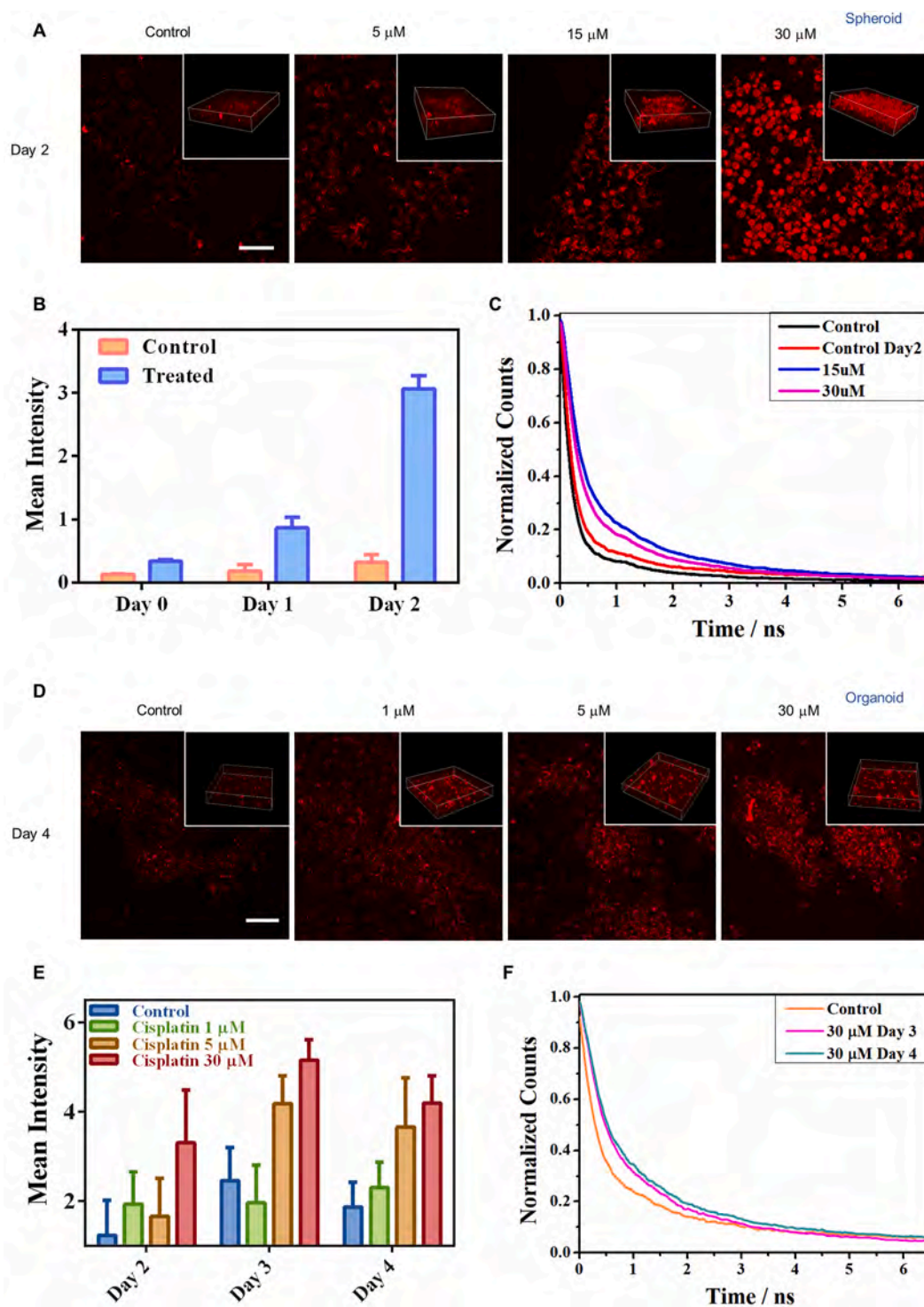
Fig. 4. Lipofuscin autofluorescence enables label-free detecting treatment responses in 3D spheroids and organoids. A Two-photon fluorescence image of lipofuscin red autofluorescence in 3D spheroids before and after treatment with cisplatin (5, 15, and 30 μM) for 2 days. The insets show the 3D view in spheroids. **B** Average TPF intensities of cells in the control group and treated group. Data are the mean ± SD of three independent experiments. **C** Lifetime traces of lipofuscin red fluorescence in the 30 μM cisplatin-treated and control cells. **D** Two-photon fluorescence images of lipofuscin red autofluorescence in organoids before and after treatment with cisplatin (1, 5, and 30 μM) for 4 days. The insets show the 3D view in organoids. **E** Average TPF intensities of cells (n = 30) in the control group and treated group. Data are the mean ± SD of three independent experiments. **F** Lifetime traces of lipofuscin red fluorescence of the 30 μM cisplatin-treated and control groups after 4 days treatment.

development, some of the skin cells in the yolk sac region of zebrafish die naturally through apoptosis, which can be visualized by the color change from green to blue (Supplementary Figs. S17B and C). At the same time, we imaged these apoptotic cells by 1120 nm excitation to detect the two-photon red fluorescence of the lipofuscin-like

fluorophore. Red autofluorescence appeared in the cells with blue color, while the live cells (cyan) exhibited almost no red fluorescence signals (Fig. 6B). These results confirmed that the lipofuscin-like fluorophore really results from the endogenous molecules and could act as a label-free apoptosis reporter in the live animal model.
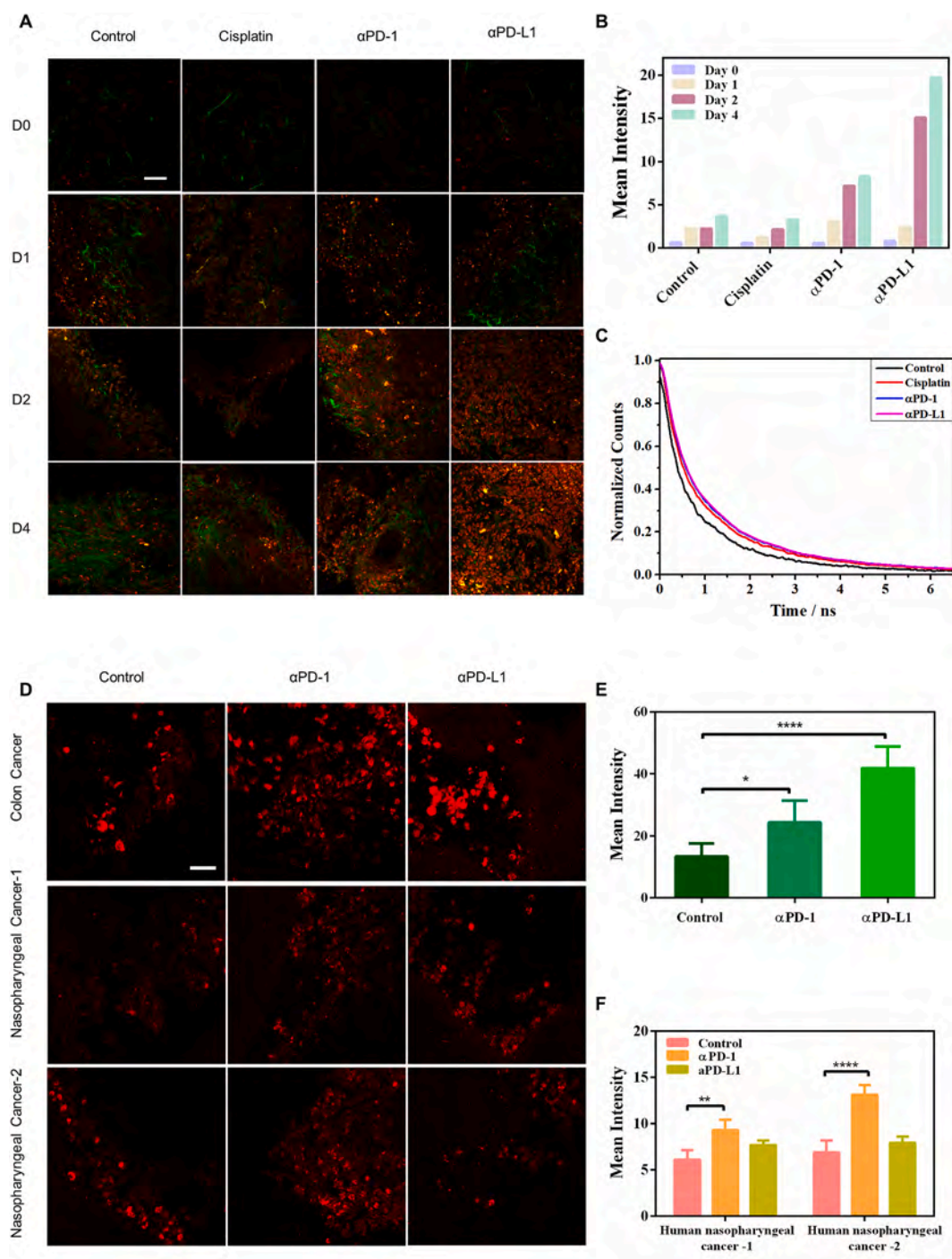
Fig. 5. Lipofuscin autofluorescence reports the responses of immune-checkpoint-blockade (ICB) therapy in mice and human 3D tumor slices (TSC). A Two-photon fluorescence microscopy ($\lambda_{ex} = 1060$ nm) of drug-induced lipofuscin fluorescence (red color) and second harmonic generation imaging of collagen networks (green color) in 3D-TSCs. Scale bar: 50 μm. **B** Average TPF intensities of lipofuscin fluorescence in 3D-TSCs treated with cisplatin, αPD-1, and αPD-L1 for four days. Lifetime traces of lipofuscin fluorescence in the control group, chemotherapy (cisplatin) group, and ICB therapy groups (αPD-1 and αPD-L1). **C** Lifetime traces of lipofuscin red fluorescence of the treated and control groups at the 4th-day post-treatment. **D** Two-photon fluorescence microscopy ($\lambda_{ex} = 1060$ nm) of ICB therapy-induced lipofuscin fluorescence (red color) in the 3D-TSC of human colon cancers (10 μg/mL αPD-1 and αPD-L1 for 7 days) and nasopharyngeal cancers (10 μg/mL αPD-1 and αPD-L1 for 3 days). Scale bar: 50 μm. **E, F** Average TPF intensities of lipofuscin fluorescence in 3D-TSCs treated with αPD-1 and αPD-L1. ***$p < 0.001$, student's *t*-test when αPD-1/αPD-L1 compared with control.

4. Discussion and conclusion

Endogenous fluorophores in cells provide a quick and label-free way to visualize drug response. Georgakoudi's group combined NAD(P)H/FAD fluorescence intensity and redox ratio of cisplatin-treated human epithelial cells to achieve a non-invasive indicator for early apoptosis [8]. In 2017, Boppart et al. utilized NADH fluorescence lifetime imaging to detect apoptosis at the cellular level [9]. Here, we advance fundamentally by discovering that senescence-specific lipofuscin-like fluorophore appears in drug-treated cells. Both apoptotic and necrotic cells showed an apparent increase in the lipofuscin-like red autofluorescence intensity, which is low in normal ones. The apoptosis and necrosis of
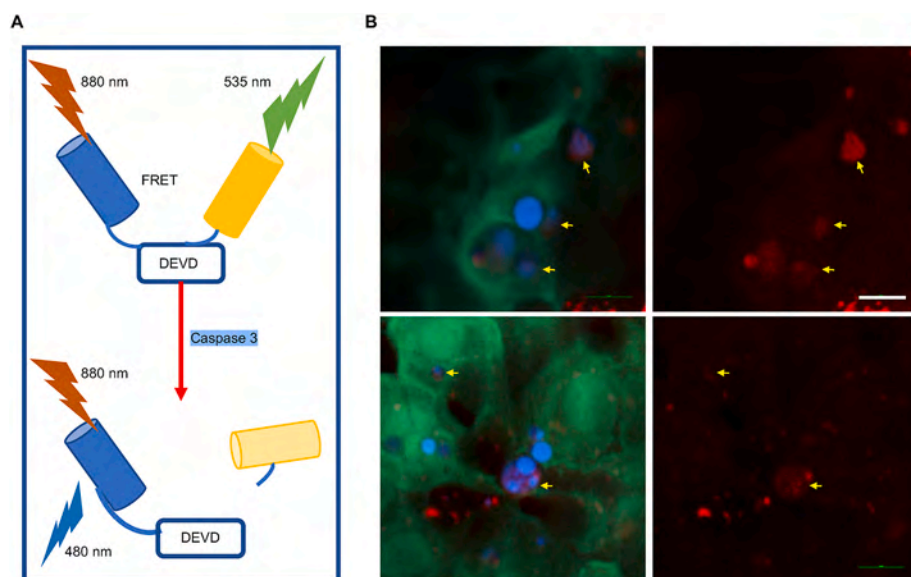
Fig. 6. **Non-invasive and label-free monitoring of the apoptotic cells during the natural skin development in the yolk sac region of the zebrafish.** **A** Principle of C3-sensor probing apoptosis in zebrafish. **B** CFP-YFP FRET imaging was used to probe the apoptotic cell during the natural skin development in the yolk sac region of the zebrafish. The DEVD-linked fusion protein (CFP/YFP) emits yellowish-green fluorescence (green color) and represents the location of live cells. The blue color indicates the CFP emmision from apoptotic ones. The yellow arrows indicate the corresponding lipofuscin fluorescence of each apoptotic cell. Scale bar: 10 μm.

cells could be further differentiated according to the lifetime and subcellular distribution of this stress-induced autofluorescence. Lipofuscin arises from the cross-linked aggregation of damaged proteins, lipids, and metal cations under ROS stress [25,36]. It has strong autofluorescence from the yellow to near-infrared spectral regions depending on the excitation wavelength [16,37]. The aged cells undergoing senescence also exhibit the hallmark autofluorescence from the lysosomal lipofuscin [38]. Under aging conditions, mitochondrial function is impaired. In addition, insufficient cellular autophagy led to incomplete removal of damaged mitochondria and increased oxidative stress. Consequently, the increased oxidative stress induces lipofuscin accumulation in lysosomes [19,39]. In contrast, enhanced mitophagy successfully inhibits lipofuscin formation [27]. These interrelated lysosomal and mitochondrial features in aging also appear in programmed cell death. The apoptosis process also involves defective mitochondria, mitophagy removal, and terminal degradation in lysosomes. In response to apoptosis stimuli, the lysosome is destabilized, and it is difficult to properly degrade the autophagosome, resulting in lipofuscin accumulation [40]. Moreover, lysosome permeabilization in different types of cell death may change the biochemical environment [41,42]. Therefore, the fluorescence lifetime of lipofuscin-like fluorophores could reflect environmental factors that affect charge relaxation in fluorophores, including solution pH values, the presence of quenchers, self-aggregation, and associations with macromolecules. That's how the fluorescence lifetime of lipofuscin-like fluorophore differentiates between cell apoptosis and necrosis.

After the discovery of apoptosis-specific fluorescence, understanding its biogenesis may provide new insights into programmed cell death and drug resistance. Its origin and the underlying mechanism are worth further exploration. We're still investigating the molecular origin and chromophore centers of this lipofuscin-like fluorescence. A potential candidate is the mitochondrial DNA (mtDNA) released from BAK/BAX macropores during apoptosis [43]. The mitochondria herniation exposed toxic mtDNA to the cytosol and then scavenged by lysosomes. Without proper degradation or removal, condensed nuclei acids in lysosomes might produce aggregation-induced fluorescence, whose red spectral profile [44] is similar to that of lipofuscin-like red autofluorescence.

In practical application, this endogenous fluorescence reporter of cell death could enhance the throughput of drug screening. Unlike conventional assays (e.g., immunofluorescence and RNA-seq) that require time-consuming fixation, exogenous staining, or destructive dissociation, our label-free methods allow non-invasive and real-time monitoring of pharmacodynamics *in situ*. It provides a chance to find the early signatures of cell death. Employing this senescence-specific contrast in multiphoton microscopy, we successfully monitor the 3D pharmacodynamics in 3D tumor models. We have validated the visualization of treatment responses in spheroids, 3D organoids, and 3D-TSC derived from animal models and patients' tumors. With preserved immune cells in 3D-TSC, we could even evaluate the responses of immune-checkpoint blockade therapy with anti-PD-1 and anti-PD-L1 antibodies. In addition, confirmed *in vivo* by the C3-sensor zebrafish model, the developmental biology planned apoptosis also shows lipofuscin-like fluorescence. These results imply that lipofuscin-like fluorescence could also report spatial-temporal apoptosis of zebrafish under drug screening.

In the future, we believe this unique apoptosis/necrosis indicating fluorescence could bring impacts on various fields of biomedical research and applications, such as mapping the heterogeneity of treatment responses in the tumor microenvironment, annotating single-cell drug resistance in spatial transcriptomics, and capturing the *in vivo* dynamics of cell death in the embryo development.

Declaration of competing interest

The authors declare the following financial interests/personal relationships which may be considered as potential competing interests: Tzu-Ming LIU has patent pending to University of Macau.

Data availability

Data will be made available on request.

Acknowledgements

Appendix A. Supplementary data

Supplementary data to this article can be found online at https://doi.org/10.1016/j.redox.2022.102578.

References

[1] S.W. Fesik, Promoting apoptosis as a strategy for cancer drug discovery, Nat. Rev. Cancer 5 (11) (2005) 876–885.

[2] B.A. Carneiro, W.S. El-Deiry, Targeting apoptosis in cancer therapy, Nat. Rev. Clin. Oncol. 17 (7) (2020) 395–417.

[3] R.M. Mohammad, et al., Broad targeting of resistance to apoptosis in cancer, in: Seminars in Cancer Biology, Elsevier, 2015.

[4] U. Fischer, K. Schulze-Osthoff, New approaches and therapeutics targeting apoptosis in disease, Pharmacol. Rev. 57 (2) (2005) 187–215.

[5] Y. Li, et al., Multifunctional gold nanoclusters-based nanosurface energy transfer probe for real-time monitoring of cell apoptosis and self-evaluating of pro-apoptotic theranostics, Anal. Chem. 88 (22) (2016) 11184–11192.

[6] K.Q. Luo, et al., Application of the fluorescence resonance energy transfer method for studying the dynamics of caspase-3 activation during UV-induced apoptosis in living HeLa cells, Biochem. Biophys. Res. Commun. 283 (5) (2001) 1054–1060.

[7] A. Lekshmi, et al., A real-time image-based approach to distinguish and discriminate apoptosis from necrosis, Curr. Protoc. Toxicol. 75 (1) (2018), 2.27. 1-2.27. 16.

[8] J.M. Levitt, et al., Intrinsic fluorescence and redox changes associated with apoptosis of primary human epithelial cells, J. Biomed. Opt. 11 (6) (2006), 064012.

[9] A.J. Bower, et al., Label-free in vivo cellular-level detection and imaging of apoptosis, J. Biophot. 10 (1) (2017) 143–150.

[10] H.-W. Wang, et al., Differentiation of apoptosis from necrosis by dynamic changes of reduced nicotinamide adenine dinucleotide fluorescence lifetime in live cells, J. Biomed. Opt. 13 (5) (2008), 054011.

[11] J. Gaspar, J. Mathieu, P. Alvarez, A rapid platform to generate lipofuscin and screen therapeutic drugs for efficacy in lipofuscin removal, Mater. Methods Technol. 10 (2016) 1–9.

[12] M.A. Yakovleva, et al., Fluorescence characteristics of lipofuscin fluorophores from human retinal pigment epithelium, Photochem. Photobiol. Sci. 19 (7) (2020) 920–930.

[13] A. Moreno-García, et al., An overview of the role of lipofuscin in age-related neurodegeneration, Front. Neurosci. 12 (2018) 464.

[14] Y. Kakimoto, et al., Myocardial lipofuscin accumulation in ageing and sudden cardiac death, Sci. Rep. 9 (1) (2019) 1–8.

[15] A. Bertolo, et al., Autofluorescence is a reliable in vitro marker of cellular senescence in human mesenchymal stromal cells, Sci. Rep. 9 (1) (2019) 1–15.

[16] M. Saif, et al., Non-invasive monitoring of chronic liver disease via near-infrared and shortwave-infrared imaging of endogenous lipofuscin, Nat. Biomed. Eng. 4 (8) (2020) 801–813.

[17] S. Jaeger, M. Duran-Frigola, P. Aloy, Drug sensitivity in cancer cell lines is not tissue-specific, Mol. Cancer 14 (1) (2015) 1–4.

[18] M.J. Kratochvil, et al., Engineered materials for organoid systems, Nat. Rev. Mater. 4 (9) (2019) 606–622.

[19] F. Xing, et al., Accelerating precision anti-cancer therapy by time-lapse and label-free 3D tumor slice culture platform, Theranostics 11 (19) (2021) 9415.

[20] X. Jiang, et al., Long-lived pancreatic ductal adenocarcinoma slice cultures enable precise study of the immune microenvironment, OncoImmunology 6 (7) (2017), e1333210.

[21] A. Ootani, et al., Sustained in vitro intestinal epithelial culture within a Wnt-dependent stem cell niche, Nat. Med. 15 (6) (2009) 701.

[22] F. Shao, et al., Enhanced protein damage clearance induces broad drug resistance in multitype of cancers revealed by an evolution drug-resistant model and genome-wide siRNA screening, Adv. Sci. 7 (23) (2020), 2001914.

[23] N. Sachs, et al., A living biobank of breast cancer organoids captures disease heterogeneity, Cell 172 (1–2) (2018) 373–386, e10.

[24] M.B. Hampton, S. Orrenius, Dual regulation of caspase activity by hydrogen peroxide: implications for apoptosis, FEBS (Fed. Eur. Biochem. Soc.) Lett. 414 (3) (1997) 552–556.

[25] A.M. Gardner, et al., Apoptotic vs. nonapoptotic cytotoxicity induced by hydrogen peroxide, Free Radic. Biol. Med. 22 (1–2) (1997) 73–83.

[26] J.R. Sparrow, et al., Fundus autofluorescence and the bisretinoids of retina, Photochem. Photobiol. Sci. 9 (11) (2010) 1480–1489.

[27] J. König, et al., Mitochondrial contribution to lipofuscin formation, Redox Biol. 11 (2017) 673–681.

[28] X. Chen, et al., Cellular pharmacology studies of shikonin derivatives, Phytother. Res. 16 (3) (2002) 199–209.

[29] M.E. Guicciardi, M. Leist, G.J. Gores, Lysosomes in cell death, Oncogene 23 (16) (2004) 2881–2890.

[30] T.G. Meijer, et al., Ex vivo tumor culture systems for functional drug testing and therapy response prediction, Future Sci. OA 3 (2) (2017), FSO190.

[31] H. Clevers, Modeling development and disease with organoids, Cell 165 (7) (2016) 1586–1597.

[32] D. Blondel, M.P. Lutolf, Bioinspired hydrogels for 3D organoid culture, CHIMIA Int. J. Chem. 73 (1) (2019) 81–85.

[33] S. Dumont, et al., Organoids of epithelial ovarian cancer as an emerging preclinical in vitro tool: a review, J. Ovarian Res. 12 (1) (2019) 1–11.

[34] S.I. Djomehri, et al., A reproducible scaffold-free 3D organoid model to study neoplastic progression in breast cancer, J. Cell Commun. Signal. 13 (1) (2019) 129–143.

[35] H. Jia, et al., Engineered sensor zebrafish for fast detection and real-time tracking of apoptosis at single-cell resolution in live animals, ACS Sens. 5 (3) (2020) 823–830.

[36] A. Terman, et al., Aging of cardiac myocytes in culture: oxidative stress, lipofuscin accumulation, and mitochondrial turnover, Ann. N. Y. Acad. Sci. 1019 (1) (2004) 70–77.

[37] G. Bottiroli, R. Ramponi, A.C. Croce, Quantitative analysis of intracellular behaviour of porphyrins, Photochem. Photobiol. 46 (5) (1987) 663–667.

[38] I. Miranda-Lorenzo, et al., Intracellular autofluorescence: a biomarker for epithelial cancer stem cells, Nat. Methods 11 (11) (2014) 1161.

[39] U.T. Brunk, A. Terman, The mitochondrial-lysosomal axis theory of aging: accumulation of damaged mitochondria as a result of imperfect autophagocytosis, Eur. J. Biochem. 269 (8) (2002) 1996–2002.

[40] U. Repnik, B. Turk, Lysosomal–mitochondrial cross-talk during cell death, Mitochondrion 10 (6) (2010) 662–669.

[41] X. Cai, et al., ROS-mediated lysosomal membrane permeabilization is involved in bupivacaine-induced death of rabbit intervertebral disc cells, Redox Biol. 18 (2018) 65–76.

[42] Y. Jin, et al., Oxidative stress-induced apoptosis of osteoblastic MC3T3-E1 cells by hydroxyapatite nanoparticles through lysosomal and mitochondrial pathways, RSC Adv. 7 (21) (2017) 13010–13018.

[43] J.S. Riley, et al., Mitochondrial inner membrane permeabilisation enables mt DNA release during apoptosis, EMBO J. 37 (17) (2018), e99238.

[44] B. Dong, et al., Superresolution intrinsic fluorescence imaging of chromatin utilizing native, unmodified nucleic acids for contrast, 113, 2016, pp. 9716–9721, 35.